

# Probing variations of the Rashba spin-orbit coupling at the nanometre scale

Jan Raphael Bindel<sup>1</sup>, Mike Pezzotta<sup>1</sup>, Jascha Ulrich<sup>2</sup>, Marcus Liebmann<sup>1</sup>, Eugene Ya. Sherman<sup>3</sup> and Markus Morgenstern<sup>1\*</sup>

**As the Rashba effect is an electrically tunable spin-orbit interaction<sup>1</sup>, it could form the basis for a multitude of applications<sup>2–4</sup>, such as spin filters<sup>3</sup>, spin transistors<sup>5,6</sup> and quantum computing using Majorana states in nanowires<sup>7,8</sup>. Moreover, this interaction can determine the spin dephasing<sup>9</sup> and antilocalization phenomena in two dimensions<sup>10</sup>. However, the real space pattern of the Rashba parameter, which critically influences spin transistors using the spin-helix state<sup>6,11,12</sup> and the otherwise forbidden electron backscattering in topologically protected channels<sup>13,14</sup>, is difficult to probe. Here, we map this pattern down to nanometre length scales by measuring the spin splitting of the lowest Landau level using scanning tunnelling spectroscopy. We reveal strong fluctuations correlated with the local electrostatic potential for an InSb inversion layer with a large Rashba coefficient ( $\sim 1$  eV Å). This type of Rashba field mapping enables a more comprehensive understanding of its fluctuations, which might be decisive towards robust semiconductor-based spintronic devices.**

The Rashba effect<sup>1</sup>, which lifts spin degeneracy by breaking inversion symmetry at surfaces and interfaces, was first probed in transport using the beating pattern in Shubnikov–de Haas oscillations<sup>15</sup> or the weak antilocalization effect<sup>16</sup>. Later, Rashba-split bands and their spin polarization were visualized by photoelectron spectroscopy<sup>17</sup>. The first successful attempts to use the Rashba effect for spin manipulation required low temperatures and found relatively small signals<sup>18–20</sup>, probably due to a D'yakonov–Perel' (DP)-type spin relaxation where each scattering event randomly changes the direction of the Rashba field, which is orthogonal to the momentum. Options to overcome this limit are to use more one-dimensional or ballistic devices<sup>21,22</sup> or a balance of the Rashba and the Dresselhaus couplings<sup>6,23</sup>, leading to a persistent spin helix with a momentum-independent spin rotation axis<sup>11,12</sup>. For such cases, where the DP mechanism is suppressed, other dephasing mechanisms limit device functionalities. An obvious candidate is the spatial fluctuation of the Rashba parameter which induces path-dependent spin rotation even on ballistic trajectories. Estimates of the dephasing rates due to this mechanism (see Methods and Supplementary Information 10) reveal that it could explain the remaining dephasing in optimized samples<sup>21–23</sup>. Interestingly, the topological protection in spin channels of two-dimensional (2D) topological insulators is probably also limited by fluctuations of the Rashba parameter in combination with

electron–electron interactions<sup>13</sup> or magnetic impurities<sup>14</sup>. However, experimental evidence of the Rashba field fluctuations has not been published so far.

A natural method to investigate electronic disorder is scanning tunnelling spectroscopy (STS)<sup>24,25</sup>, which has already revealed fingerprints of the Rashba effect in two-dimensional electron systems (2DES)<sup>26–28</sup>, but so far without probing its spatial pattern.

Here, we use an InSb 2DES, produced by Cs adsorbates on the (110) surface (see Methods), as a model system to probe the Rashba parameter  $\alpha_R$  in real space. STS in a perpendicular magnetic field  $B$  reveals a nonlinear spin splitting of the Landau levels (LL), which fits to the Rashba model at intermediate  $B = 3–7$  T, whereas exchange enhancement<sup>29,30</sup> dominates at higher  $B$ . Thus, the spin splitting at intermediate  $B$  can be used to trace the Rashba parameter  $\alpha_R(\mathbf{R})$  as a function of position  $\mathbf{R}$ , revealing that  $\alpha_R(\mathbf{R})$  fluctuates spatially between 0.4 eV Å and 1.6 eV Å. The  $\alpha_R(\mathbf{R})$  map with a correlation length of 30 nm exhibits a strong correlation with the electrostatic potential of the 2DES  $V_{2D}(\mathbf{R})$ , as mapped by the spin-averaged LL energy. The observed fluctuations of  $\alpha_R(\mathbf{R})$  are in agreement with analytic estimates.

The sample is sketched in Fig. 1a. By adsorbing Cs on p-type InSb(110), the valence and conduction bands are bent down towards the surface, forming an inversion layer with one occupied subband (Fig. 1b)<sup>28</sup>. The Cs coverage (1.8% of a monolayer) is low enough to barely disturb the mapping of the 2DES by STS, but large enough such that the disorder is dominated by the more loosely spaced bulk acceptors<sup>28,29,31,32</sup>. A strong electric field  $|\mathbf{E}| \approx 3 \times 10^7$  V m<sup>-1</sup> within the 2DES results from acceptor doping<sup>28</sup>, which in combination with the large atomic numbers of In and Sb leads to a large  $\alpha_R$ . Figure 1c shows the spin-split LLs of this 2DES according to the Bychkov–Rashba model<sup>1</sup>. One recognizes crossing points of opposite spin levels (dashed ellipses) and a nonlinearity of the spin splitting at low  $B$ . Figure 1d shows this splitting for different  $\alpha_R$ , while keeping all other parameters identical. Different couplings naturally lead to different nonlinearities, offering an elegant method to locally determine  $\alpha_R$ . Although  $\alpha_R$  is a strictly local parameter, the measured spin splitting is related to wavefunctions, such that the spatial resolution of the method is limited to approximately the cyclotron radius, being smallest for the lowest Landau level  $LL_0$ . For smooth  $V_{2D}(\mathbf{R})$  with respect to the magnetic length  $l_B = \sqrt{\hbar/eB}$  (cyclotron radius of  $LL_0$ ,  $\hbar$ : reduced Planck constant,  $e$ : electron charge)—that is, the guiding centre dynamics can be described semiclassically—one

<sup>1</sup>II. Institute of Physics B and JARA-FIT, RWTH Aachen University, D-52074 Aachen, Germany. <sup>2</sup>Institute for Quantum Information and JARA-FIT, RWTH Aachen University, D-52074 Aachen, Germany. <sup>3</sup>Department of Physical Chemistry, University of the Basque Country UPV-EHU and IKERBASQUE, Basque Foundation for Science, 48080 Bilbao, Spain. \*e-mail: mmorgens@physik.rwth-aachen.de

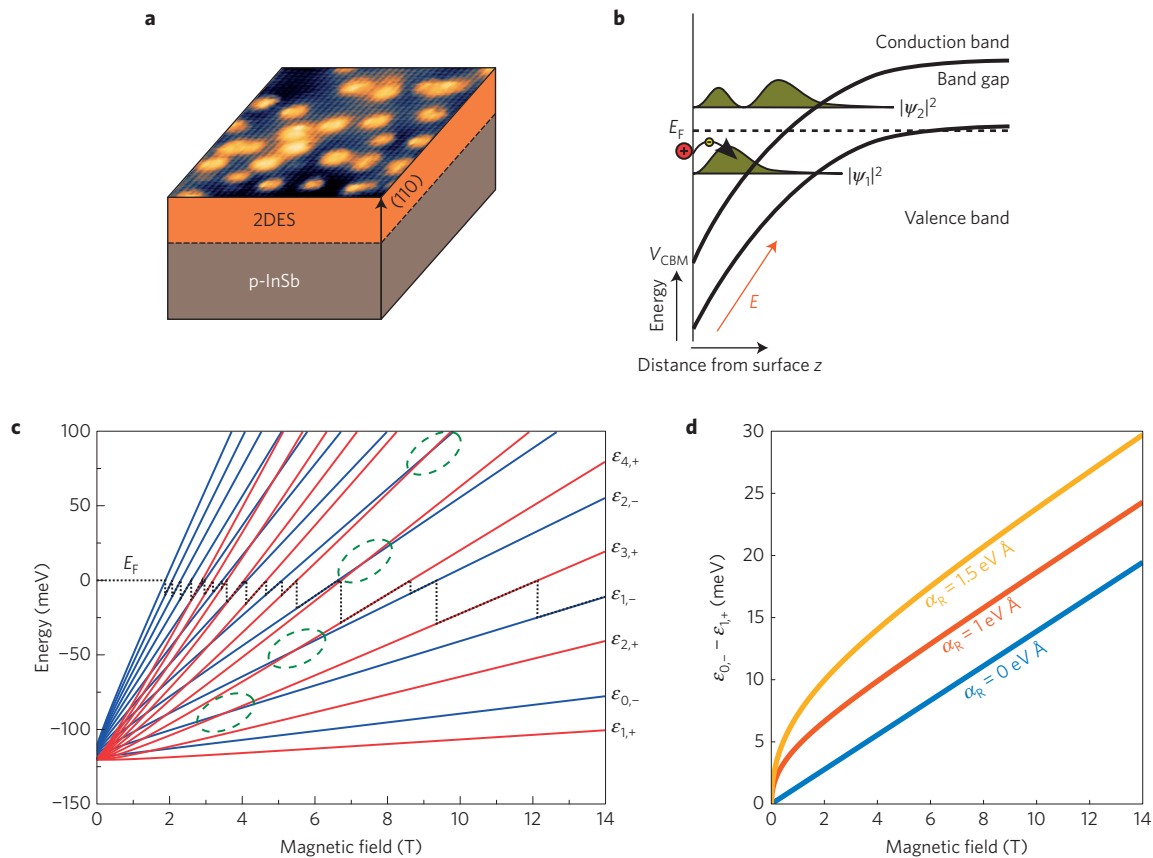


**Figure 1 | Rashba parameter from spin splitting of Landau levels.** **a**, Sketch of the sample with the two-dimensional electron system (2DES) at the surface and the conducting p-InSb bulk. An STM image of Cs/InSb(110) with atomic resolution showing Cs atoms (bright dots) on top of the lines of In atoms is projected on the surface ( $20 \times 20 \text{ nm}^2$ ,  $V = 300 \text{ mV}$ ,  $I = 30 \text{ pA}$ ,  $T = 8 \text{ K}$ ). **b**, Band structure of the 2DES perpendicular to the surface, as resulting from a Poisson calculation. Confined squared wavefunctions ( $|\psi_1|^2$ ,  $|\psi_2|^2$ ) are sketched in olive. Adsorbed Cs atoms act as donors. **c**, B-field dependence of the energy levels of one 2DES subband using  $\alpha_R = 0.7 \text{ eV \AA}$ ,  $g = -21$ ,  $m^* = 0.03m_e$  (average values from the potential area shown in Fig. 3a). Opposite spin contributions are marked in blue and red. The Fermi level is shown as a dotted line, using  $n = 1.5 \times 10^{16} \text{ m}^{-2}$ . Crossing points of different spin levels are highlighted by dashed ellipses. Labels on the right are used in equation (1). **d**, Splitting of the two lowest energy levels for different Rashba parameters  $\alpha_R$ ,  $g = -21$ ,  $m^* = 0.03m_e$ .

finds the energies  $\varepsilon_{n,\lambda}(B, \mathbf{R})$  for different LLs  $n$  and spin labels  $\lambda = +, -$  (ref. 33):

$$\varepsilon_{n,\lambda}(B, \mathbf{R}) = \hbar\omega_c \left[ n - \frac{\lambda}{2} \sqrt{\left(1 - \frac{gm^*}{2m_e} + \frac{V_{2D,n}(\mathbf{R}) - V_{2D,n-1}(\mathbf{R})}{\hbar\omega_c}\right)^2 + n \left(\frac{2\sqrt{2}\alpha_R(\mathbf{R})}{\hbar\omega_c l_B}\right)^2} \right] + \frac{V_{2D,n-1}(\mathbf{R}) + V_{2D,n}(\mathbf{R})}{2} \quad (1)$$

$$V_{2D,n}(\mathbf{R}) = \iint V_{2D}(\mathbf{R} + \mathbf{r}) F_n(\mathbf{r}) d^2\mathbf{r} \quad (2)$$

provided that Landau level mixing by disorder can be neglected—that is,  $\sigma_{V_{2D}} < \hbar\omega_c$ . Here,  $F_n(\mathbf{r})$  is the kernel of the  $n$ th LL wavefunction (Supplementary Information 1),  $m^*$  is the effective mass,  $g$  is the  $g$ -factor,  $\omega_c = eB/m^*$  is the cyclotron frequency,  $m_e$  is the electron mass and  $\sigma_{V_{2D}}$  is the standard deviation of the histogram of  $V_{2D}(\mathbf{R})$ . With equations (1) and (2), we can determine

$\alpha_R(\mathbf{R})$ , using  $\Delta E_{SS}(B, \mathbf{R}) = \varepsilon_{0,-}(B, \mathbf{R}) - \varepsilon_{1,+}(B, \mathbf{R})$ , if  $V_{2D}(\mathbf{R})$ ,  $g$  and  $m^*$  are also known. The error for such an  $\alpha_R(\mathbf{R})$  determination originates mainly from the neglected higher-order derivatives of  $V_{2D}(\mathbf{R})$  within equation (1), and is on average 5% for the probed 2DES (Supplementary Information 2 and 6).

Figure 2a shows the density of states (DOS)—that is, the spatially averaged local density of states (LDOS)—of the 2DES at  $B = 7 \text{ T}$ . The characteristic beating pattern of the LLs found previously<sup>28</sup> is used to estimate the average Rashba parameter  $\bar{\alpha}_R$  by comparison with the fitting lines. The best agreement is found for  $\bar{\alpha}_R = 0.7 \text{ eV \AA}$ , corroborating the earlier results<sup>28</sup>. Discrepancies between fit and data at higher LLs are due to the neglected nonparabolicity of the conduction band<sup>28</sup>. The observed strong dip at the Fermi level  $E_F$  in the experiment is related to the well-known Coulomb gap<sup>29,34</sup>.

To extract the local Rashba parameter  $\alpha_R(\mathbf{R})$ , we record local LL fans. Figure 2b shows the measured LDOS of a single spatial point at different energies and  $B$ . LLs and spin levels of two subbands are discernible as marked. The individual levels collectively undulate with  $B$ , which we ascribe to the undulation of all LLs with respect to  $E_F$  to maintain the fixed carrier density  $n$  and, to a lesser extent, to exchange enhancement<sup>29</sup>. Reproducible instabilities in the spectroscopy are observed at distinct  $B$  (crosses, Supplementary Information 3). Here, the conductance at  $E_F$  drops below  $\sim 3 \text{ pS}$ —that is, an insulating sample area close to integer

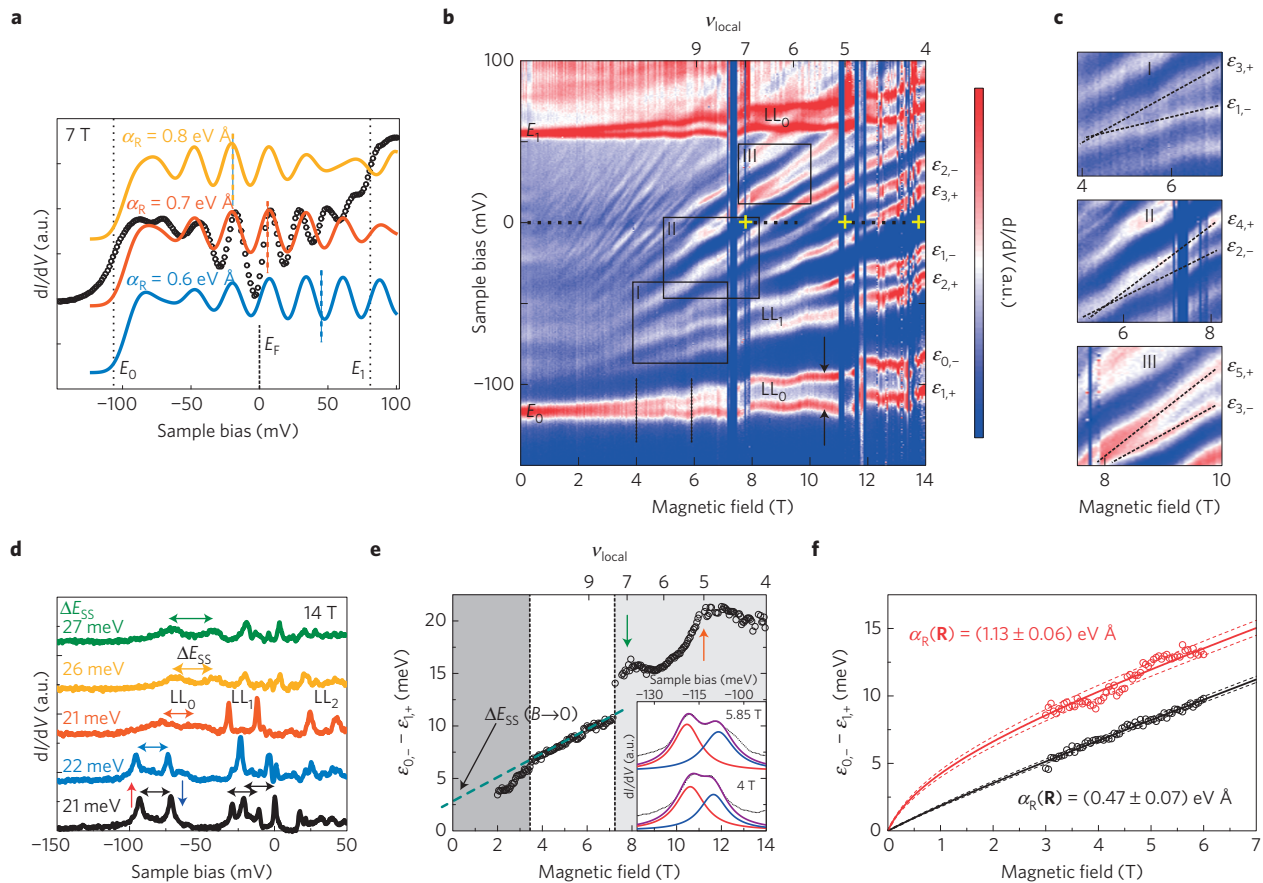


**Figure 2 | Local Rashba parameter deduced by STS.** **a**, Circles: spatially averaged differential conductance from  $150 \times 150 \text{ nm}^2$  area ( $35 \times 35$  pixel) of Cs/InSb(110) ( $V_{\text{stab}} = 300 \text{ mV}$ ,  $I_{\text{stab}} = 0.2 \text{ nA}$ ,  $V_{\text{mod}} = 3.5 \text{ mV}$ ,  $T = 400 \text{ mK}$ ,  $B = 7 \text{ T}$ ). Dotted lines mark  $E_0$  and  $E_1$ , the onsets of the two different subbands. Full lines: calculated density of states for different  $\alpha_R$  as marked. Best correspondence of the beating antinode is found for  $\alpha_R \approx 0.7 \text{ eV \AA}$ . We use constant  $m^* = 0.03m_e$ ,  $g = -21$  and a width of the LL peaks directly taken from the distribution of  $V_{2D}(\mathbf{R})$  (Fig. 3e). **b**,  $dI/dV(V)$  measurement at a single position within a potential minimum of the 2DES recorded at changing  $B$  ( $V_{\text{stab}} = 50 \text{ mV}$ ,  $I_{\text{stab}} = 0.1 \text{ nA}$ ,  $V_{\text{mod}} = 0.75 \text{ mV}$ ,  $T = 7.5 \text{ K}$ ).  $LL_n$  mark the Landau levels of the lowest subband  $E_0$  and the first subband  $E_1$ ,  $\epsilon_{n,\pm}$  mark levels of  $LL_n$  according to equation (1). The local filling factor  $\nu_{\text{local}}$ , marked on top, results from counting all levels up to  $E_F$ . The yellow crosses mark integer filling factors. Around these filling factors spectroscopy becomes unstable due to low conductance ( $\sim 3 \text{ pS}$ ). These areas are artificially coloured blue (Supplementary Information 3). Black arrows mark the spin levels used in **e** and **f**. Boxes with roman numbers mark the zoom regions shown in **c**. **c**, Zooms into **b** with overlaid guides to the eye (dashed lines), which follow two levels crossing at finite  $B$ . **d**, Differential conductance recorded at different positions ( $V_{\text{stab}} = 300 \text{ mV}$ ,  $I_{\text{stab}} = 0.2 \text{ nA}$ ,  $V_{\text{mod}} = 0.7 \text{ mV}$ ,  $T = 400 \text{ mK}$ ,  $B = 14 \text{ T}$ ). Landau levels  $LL_n$  and spin splittings  $\Delta E_{SS}$ , marked by horizontal double arrows, are indicated. The resulting spin splitting of  $LL_0$  is marked on the left. Note that multiple peaks appear for higher LLs and that the sharpest  $LL_0$  levels are found at the lowest energies. **e**, Circles: energy difference of the two lowest energy levels of **b** (marked by black arrows in **b**). Dashed line extrapolates the nearly linear slope between  $3.4 \text{ T}$  and  $7.2 \text{ T}$  towards  $0 \text{ T}$  as marked by  $\Delta E_{SS}^0 (B \rightarrow 0)$ . Green and orange arrows belong to  $\nu_{\text{local}} = 5$  and  $\nu_{\text{local}} = 7$ , respectively. Inset:  $dI/dV$  curves from the low-energy part of **b** as marked (dots) with fit line (violet) consisting of two Lorentzian peaks (red, blue). The energy difference between the maxima of the two Lorentzians is shown as circles in the main image. **f**, Circles:  $LL_0$  splitting determined between  $3 \text{ T}$  and  $6 \text{ T}$  at two different positions (red, black) as marked by crosses in Fig. 3a–d. Full lines: fit according to the Rashba model with resulting local Rashba parameter  $\alpha_R(\mathbf{R})$  marked. Dashed lines: 65% confidence interval of the fits with corresponding values of  $\pm \Delta \alpha_R(\mathbf{R})$  marked.

filling factors prohibits current flow at these values of  $B$ . We ascribe the slight suppression of LDOS around  $E_F$  again to the Coulomb gap<sup>29,34</sup>.

Multiple crossings of levels are present, for example, in the boxes marked I–III enlarged in Fig. 2c. The dashed lines (guides to the eye) reveal that the marked levels cross away from  $B = 0 \text{ T}$ , such that they cannot belong to simple Landau and spin energies, both being linear in  $B$  and crossing at  $B = 0 \text{ T}$ . A natural way to explain the crossings is the Rashba effect and, indeed, some of the crossings appear at values of  $B$  similar to those in the calculations (Fig. 1c). Discrepancies, most obvious at lower  $B$ , are attributed to the local confinement within the potential minimum, where the data are recorded. This complication hampers the use of the crossings for an accurate determination of  $\alpha_R$ .

Instead, we use the  $B$ -nonlinearity of the  $LL_0$  spin splitting  $\Delta E_{SS}(B, \mathbf{R})$ . Figure 2d shows the measured LDOS at several  $\mathbf{R}$  and  $B = 14 \text{ T}$ . Double peaks for  $LL_0$ , and more complicated structures for higher LLs, are found. The complex peak structures appear away from the extrema of  $V_{2D}(\mathbf{R})$  owing to the nodal structure of the LL wavefunctions<sup>31</sup>. The splitting  $\Delta E_{SS}(B, \mathbf{R})$  determined from fitting two Lorentzians to the pair of peaks of  $LL_0$  is indicated. It increases for higher average energy—that is, for higher  $V_{2D}(\mathbf{R})$ . This is opposite to the expectation from the nonparabolicity of  $g(V_{2D})$ , which decreases with increasing  $V_{2D}$  (ref. 28). Furthermore, a fluctuating peak width is observed, which will be discussed elsewhere.

Figure 2e shows  $\Delta E_{SS}(B, \mathbf{R})$  as deduced from Fig. 2b using Lorentzian fits (inset). Above  $B = 7 \text{ T}$ ,  $\Delta E_{SS}$  oscillates, exhibiting

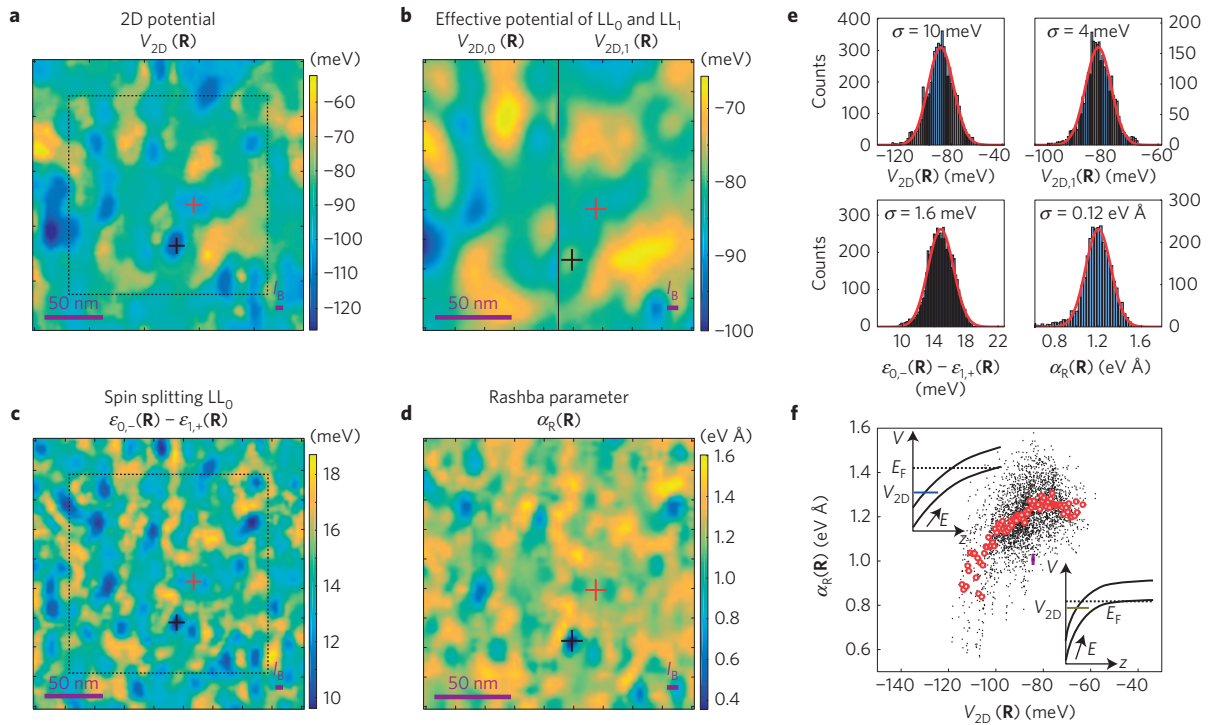


**Figure 3 | Mapping of Rashba parameter and comparison with potential map.** **a**, Map of the potential energy  $V_{2D}(\mathbf{R})$  of the 2DES, which is  $(\epsilon_{0,-}(\mathbf{R}) + \epsilon_{1,+}(\mathbf{R}))/2$  as resulting from fits of  $dI/dV$  data as described in Methods and shown in the inset of Fig. 2e ( $V_{\text{stab}} = 50$  mV,  $I_{\text{stab}} = 0.1$  nA,  $V_{\text{mod}} = 1.5$  mV,  $T = 400$  mK,  $B = 6$  T). Black and red cross show positions of curves in Fig. 2f drawn in the same colour. Black dotted square indicates the areas shown in **b** and **d**. The correlation length of the potential is  $L_{V_{2D}V_{2D}} = 50$  nm (Supplementary Information 5). There is no correlation to the Cs distribution exhibiting interatomic distances of only 4 nm. **b**,  $V_{2D,0}(\mathbf{R})$  (left) and  $V_{2D,1}(\mathbf{R})$  (right) at  $B = 6$  T calculated from the respective area of the  $V_{2D}(\mathbf{R})$  map according to equation (2). **c**,  $LL_0$  splitting ( $\Delta E_{SS}$ ) map at  $B = 6$  T. **d**, Spatially resolved Rashba parameter  $\alpha_R(\mathbf{R})$  determined by using equation (1), the 2D potential from **a** and the spin splitting map from **c**. **e**, Histograms of the maps shown in **a-d**. Gaussian fits (red lines) are added with  $\sigma$ -values indicated. **f**, Black dots:  $\alpha_R(\mathbf{R})$  from **d** plotted as a function of  $V_{2D}(\mathbf{R})$  from **a**, always using the same position  $\mathbf{R}$ . Red circles: averaged Rashba parameter across a  $V_{2D}(\mathbf{R})$  interval of 0.5 meV. Purple error bar indicates the typical error bars of  $V_{2D}$  and  $\alpha_R$ , revealing that the scatter in  $\alpha_R$  is significantly larger than the error bar. Insets: sketch of band bending at a lateral position  $(x, y)$  of low (top left) and high local acceptor density (bottom right). The coloured line marks the potential  $V_{2D}(x, y)$  determined by folding the band course  $V(x, y, z)$  along the vertical direction  $z$ , with the vertical shape of the probability distribution of the lowest subband of the 2DES  $|\Psi_1|^2$  (see Fig. 1b), according to  $V_{2D}(x, y) = \int_0^\infty V(x, y, z) |\Psi_1(z)|^2 dz$ . This is mimicking the measured  $V_{2D}(\mathbf{R})$  in **a**.

maxima at odd filling factors, as expected for exchange enhancement<sup>29,30</sup>. Because the exchange interaction depends exponentially on the overlap of the wavefunctions, which roughly scales with  $l_B \propto \sqrt{1/B}$ , it decays rapidly at lower fields, being below 1 meV for  $B < 6$  T (ref. 29). Accordingly, oscillations of  $\Delta E_{SS}$  are barely discernible at  $B < 7$  T. Instead a largely linear  $\Delta E_{SS}$  is observed at 3–7 T, decaying more rapidly at lower fields, as in the curves of Fig. 1d. Extrapolating the linear part to  $B = 0$  T (dashed line) reveals an offset of  $\Delta E_{SS}^0 \sim 2.5$  meV. Taylor expansion of equation (1) for large  $B$  using  $V_{2D}(\mathbf{R}) = \text{constant}$ —that is,  $V_{2D,n}(\mathbf{R}) = V_{2D,n-1}(\mathbf{R})$  (ref. 33)—reveals that the offset is given by  $\Delta E_{SS}^0(B \rightarrow 0) = 4\alpha_R^2 m^* / \hbar^2 (2 - gm^*/m_e)$ , resulting in  $\alpha_R \approx 0.65$  eV Å close to  $\bar{\alpha}_R = 0.7$  eV Å from Fig. 2a. Figure 2f shows the fitted  $\Delta E_{SS}(B, \mathbf{R})$  for two different potential minima, indicated by crosses in Fig. 3a–d. For the fit, we also consider the  $V_{2D,n}(\mathbf{R})$  terms of equation (1) deduced from the potential  $V_{2D,n}(\mathbf{R})$  of Fig. 3a (see below). The effective mass is determined from the  $B$ -field-dependent slope of the energy splitting between  $LL_0$  and  $LL_1$  (Supplementary Information 6). The  $g$ -factor then results from the relation  $g(V_{2D})m^*(V_{2D}) = g_0m_0^*$ , with  $g_0 = -51$  and  $m_0^* = 0.0135m_e$  at the conduction band minimum, leaving  $\alpha_R$  as the only fit parameter<sup>28</sup>. The two resulting  $\alpha_R$  values differ by a factor of two, indicating strong spatial  $\alpha_R$  fluctuations.

We can easily rule out that the spatial fluctuation of  $g$  is responsible for the differences, as the curve probed at  $V_{2D}(\mathbf{R}) = -121$  meV (black) should have a larger  $g$ -factor than that

probed at  $V_{2D}(\mathbf{R}) = -101$  meV (red), in contrast to the experimental observation. Exchange enhancement is also much weaker than the obtained differences in  $\Delta E_{SS}$ .

Having established that  $\alpha_R(\mathbf{R})$  can be deduced from  $\Delta E_{SS}$ , we map  $\alpha_R(\mathbf{R})$ . A precise determination also requires  $V_{2D}(\mathbf{R})$  maps (equation (1)). Therefore, we plot the mean energy of the two  $LL_0$  peaks representing  $V_{2D}(\mathbf{R})$  (Fig. 3a). The resulting potential fluctuates by about  $\pm 10$  meV, with a correlation length  $L_{V_{2D}V_{2D}} = 50$  nm. Convolving with the  $LL$  wavefunction kernel (equation (2)) leads to the  $V_{2D}(\mathbf{R})$  maps in Fig. 3b, which are slightly smoother than Fig. 3a. Figure 3c shows the  $\Delta E_{SS}(B, \mathbf{R})$  map at  $B = 6$  T and Fig. 3d shows the resulting  $\alpha_R(\mathbf{R})$  map according to equation (1). The  $\Delta E_{SS}(B, \mathbf{R})$  and  $\alpha_R(\mathbf{R})$  maps exhibit similar patterns, but differ in details.

Notably,  $\alpha_R(\mathbf{R})$  fluctuates between 0.4 eV Å and 1.6 eV Å—that is, by a factor of four. It exhibits a giant  $\bar{\alpha}_R = 1.2$  eV Å, a root-mean-square fluctuation  $\delta\alpha_R = 0.15$  eV Å (Fig. 3e), and a correlation length of  $L_{\alpha_R\alpha_R} = 30$  nm, being larger than  $l_B$ , but smaller than  $L_{V_{2D}V_{2D}}$  (Supplementary Information 5). The latter is due to the stronger relative fluctuations of the  $E$ -field of a distribution of Coulomb impurities with respect to the electrostatic potential (Supplementary Information 9). In Methods, we show that  $\delta\alpha_R$  and  $L_{\alpha_R\alpha_R}$  are reasonably reproduced by a fitting-parameter-free analytic model using the experimental densities of Cs and bulk acceptors.

It is known that  $\alpha_R(\mathbf{R})$  depends mostly on the local electric field  $\mathbf{E}(\mathbf{R})$  perpendicular to the 2DES<sup>1</sup>, which is not measurable by STS. However, comparing  $\alpha_R(\mathbf{R})$  with the measured  $V_{2D}(\mathbf{R})$ , we find a monotonic relation after averaging all  $\alpha_R(\mathbf{R})$  values belonging to the same  $V_{2D}$  (red circles in Fig. 3f). This can be rationalized by numerically calculating the electric field and the potential from randomly distributed Cs surface donors and bulk acceptors (Supplementary Information 7). It turns out, as found previously<sup>32</sup>, that the potential from the Cs surface donors is spatially rather fixed ( $\delta V_{2D} = 1.5$  meV) whereas the potential fluctuations are dominated by the more distant acceptors ( $\delta V_{2D} = 25$  meV). Thus, a stronger electric field (steeper slope of the potential) automatically correlates with a larger  $V_{2D}(\mathbf{R})$  (potential folded with the vertical wavefunction of the 2DES). However, the remaining scatter of  $\alpha_R$  at given  $V_{2D}$  ( $\bar{\sigma}_{\alpha_R}(V_{2D}) = 0.12$  eV Å) is much larger than the error bar of the  $\alpha_R$  determination ( $\bar{\sigma}_{\alpha_R} = 0.02$  eV Å). This is straightforwardly explained by the remaining scatter in the relation between the simulated  $V_{2D}(\mathbf{R})$  and  $\mathbf{E}(\mathbf{R})$  (Supplementary Information 8). Notice that the spin-splitting map exhibits more spatial detail than the potential map, because Coulomb impurities imply steeper electric fields ( $\propto 1/r^2$ ) than potentials  $\propto (1/r)$  (Supplementary Information 9).

Finally, we estimate the spin dephasing length  $l_{\text{spin}}$  and the spin diffusion length  $l_s$  from the data of Fig. 3d—that is, we consider only the fluctuations of  $\alpha_R$  for spin dephasing<sup>35</sup> (see Methods). We obtain  $l_{\text{spin}} \approx 250$  nm, which is slightly larger than the mean free path in this particular system ( $l_{\text{MFP}} \approx 20$ –200 nm), such that  $l_s = \sqrt{l_{\text{spin}} l_{\text{MFP}}/2} \approx 50$ –150 nm, being similar to the spin precession length (80 nm). This type of spin dephasing becomes decisive, for example, if the DP mechanism is avoided, as in ballistic<sup>21,22</sup> or spin-helix<sup>6,11,12,23</sup> transistors. For some of these systems, we can estimate  $l_{\text{spin}} \approx 23$   $\mu\text{m}$  (ref. 21), 60  $\mu\text{m}$  (ref. 23), or 500  $\mu\text{m}$  (ref. 22) and  $l_s \approx 4$   $\mu\text{m}$  (refs 21,23) or 20  $\mu\text{m}$  (ref. 22), which is compatible with the remaining signs of dephasing there (Supplementary Information 10). In particular, whereas DP and Elliott–Yafet dephasing disappear in ballistic channels, the fluctuations of  $\alpha_R(\mathbf{R})$  still cause dephasing as long as the conducting channel is wider than  $L_{\alpha_R}$ , being, for example, 80 nm (ref. 21) or 450 nm (ref. 22) in typical devices. Consequently, a detailed understanding of  $\alpha_R(\mathbf{R})$  fluctuations, as uniquely provided by our method, becomes crucial for these prospective devices, in particular when it comes to assessing reliability issues in spin transistor networks.

## Methods

Methods, including statements of data availability and any associated accession codes and references, are available in the [online version of this paper](#).

Received 15 February 2016; accepted 21 April 2016;  
published online 16 May 2016; corrected online 7 September 2016

## References

- Bychkov, Y. A. & Rashba, E. I. Properties of a 2D electron gas with lifted spectral degeneracy. *JETP Lett.* **39**, 78–81 (1984).
- Zutic, I., Fabian, J. & Das Sarma, S. Spintronics: fundamentals and applications. *Rev. Mod. Phys.* **76**, 323–410 (2004).
- Koga, T., Nitta, J., Takayanagi, H. & Datta, S. Spin-filter device based on the Rashba effect using a nonmagnetic resonant tunneling diode. *Phys. Rev. Lett.* **88**, 126601 (2002).
- Awschalom, D. D. & Flatte, M. E. Challenges for semiconductor spintronics. *Nature Phys.* **3**, 153–159 (2007).
- Datta, S. & Das, B. Electronic analog of the electrooptic modulator. *Appl. Phys. Lett.* **56**, 665–667 (1990).
- Schliemann, J., Carlos Egués, J. & Loss, D. Nonballistic spin-field-effect transistor. *Phys. Rev. Lett.* **90**, 146801 (2003).
- Mourik, V. *et al.* Signatures of Majorana fermions in hybrid superconductor–semiconductor nanowire devices. *Science* **336**, 1003–1007 (2012).
- Nadj-Perge, S. *et al.* Observation of Majorana fermions in ferromagnetic atomic chains on a superconductor. *Science* **346**, 602–607 (2014).
- D'yakonov, M. I. & Perel', V. I. Spin relaxation of conduction electrons in noncentrosymmetric semiconductors. *Sov. Phys. Solid State* **13**, 3023–3026 (1972).
- Sheng, L., Sheng, D. N. & Ting, C. S. Spin-Hall effect in two-dimensional electron systems with Rashba spin-orbit coupling and disorder. *Phys. Rev. Lett.* **94**, 016602 (2005).
- Koralek, J. D. *et al.* Emergence of the persistent spin helix in semiconductor quantum wells. *Nature* **458**, 610–613 (2009).
- Sasaki, A. *et al.* Direct determination of spin-orbit interaction coefficients and realization of the persistent spin helix symmetry. *Nature Nanotech.* **9**, 703–709 (2014).
- Stroem, A., Johannesson, H. & Japaridze, G. I. Edge dynamics in a quantum spin Hall state: effects from Rashba spin-orbit interaction. *Phys. Rev. Lett.* **104**, 256804 (2010).
- Kimme, L., Rosenow, B. & Brataas, A. Backscattering in helical edge states from a magnetic impurity and Rashba disorder. *Phys. Rev. B* **93**, 081301 (2016).
- Nitta, J., Akazaki, T. & Takayanagi, H. Gate control of spin-orbit interaction in an inverted  $\text{In}_{0.53}\text{Ga}_{0.47}\text{As}/\text{In}_{0.52}\text{Al}_{0.48}\text{As}$  heterostructure. *Phys. Rev. Lett.* **78**, 1335–1338 (1997).
- Koga, T., Nitta, J., Akazaki, T. & Takayanagi, H. Rashba spin-orbit coupling probed by the weak antilocalization analysis in  $\text{InAlAs}/\text{InGaAs}/\text{InAlAs}$  quantum wells as a function of quantum well asymmetry. *Phys. Rev. Lett.* **89**, 046801 (2002).
- LaShell, S., McDougall, B. A. & Jensen, E. Spin splitting of an Au(111) surface state band observed with angle resolved photoelectron spectroscopy. *Phys. Rev. Lett.* **77**, 3419–3422 (1996).
- Koo, H. C. *et al.* Control of spin precession in a spin-injected field effect transistor. *Science* **325**, 1515–1518 (2009).
- Wunderlich, J. *et al.* Spin Hall effect transistor. *Science* **330**, 1801–1804 (2010).
- Bethausen, C. *et al.* Spin-transistor action via tunable Landau-Zener transitions. *Science* **337**, 324–327 (2012).
- Choi, W. Y. *et al.* Electrical detection of coherent spin precession using the ballistic intrinsic spin Hall effect. *Nature Nanotechnol.* **10**, 666–670 (2015).
- Chuang, P. *et al.* All-electric all-semiconductor spin field-effect transistors. *Nature Nanotech.* **10**, 35–39 (2015).
- Faniel, S., Matsuura, T., Mineshige, S., Sekine, Y. & Koga, T. Determination of spin-orbit coefficients in semiconductor quantum wells. *Phys. Rev. B* **83**, 115309 (2011).
- Richardella, A. *et al.* Visualizing critical correlations near the metal-insulator transition in  $\text{Ga}_{1-x}\text{Mn}_x\text{As}$ . *Science* **327**, 665–669 (2010).
- Beidenkopf, H. *et al.* Spatial fluctuations of helical Dirac fermions on the surface of topological insulators. *Nature Phys.* **7**, 939–943 (2011).
- Ast, C. R. *et al.* Local detection of spin-orbit splitting by scanning tunneling spectroscopy. *Phys. Rev. B* **75**, 201401 (2007).
- El-Kareh, L., Sessi, P., Bathon, T. & Bode, M. Quantum interference mapping of Rashba-split Bloch states in  $\text{Bi}/\text{Ag}(111)$ . *Phys. Rev. Lett.* **110**, 176803 (2013).
- Becker, S., Liebmann, M., Mashoff, T., Pratzner, M. & Morgenstern, M. Scanning tunneling spectroscopy of a dilute two-dimensional electron system exhibiting Rashba spin splitting. *Phys. Rev. B* **81**, 155308 (2010).
- Becker, S. *et al.* Probing electron-electron interaction in quantum Hall systems with scanning tunneling spectroscopy. *Phys. Rev. Lett.* **106**, 156805 (2011).
- Ando, T. & Uemura, Y. Theory of oscillatory  $g$  factor in an MOS inversion layer under strong magnetic fields. *J. Phys. Soc. Jpn* **37**, 1044–1052 (1974).
- Hashimoto, K. *et al.* Robust nodal structure of Landau level wave functions revealed by Fourier transform scanning tunneling spectroscopy. *Phys. Rev. Lett.* **109**, 116805 (2012).
- Morgenstern, M. *et al.* Direct comparison between potential landscape and local density of states in a disordered two-dimensional electron system. *Phys. Rev. Lett.* **89**, 136806 (2002).
- Hernangómez-Pérez, D., Ulrich, J., Florens, S. & Champel, T. Spectral properties and local density of states of disordered quantum Hall systems with Rashba spin-orbit coupling. *Phys. Rev. B* **88**, 245433 (2013).
- Masutomi, R. & Okamoto, T. Adsorbate-induced quantum Hall system probed by scanning tunneling spectroscopy combined with transport measurements. *Appl. Phys. Lett.* **106**, 251602 (2015).
- Glazov, M. M., Sherman, E. Ya. & Dugaev, V. K. Two-dimensional electron gas with spin-orbit coupling disorder. *Phys. E* **42**, 2157–2177 (2010).

## Acknowledgements

We appreciate helpful discussions with D. Hernangómez-Pérez, S. Florens, T. Champel, S. Becker, A. Georgi, C. Saunus, N. M. Freitag, M. M. Glazov, V. K. Dugaev and R. Winkler. Financial support by the German Science foundation via MO 858/11-2 and INST 222/776-1 is gratefully acknowledged. J.U. acknowledges financial support via the

Alexander von Humboldt-Stiftung. The work of E.Y.S. was supported by the University of the Basque Country UPV/EHU under program UFI 11/55, Spanish Ministry of Economics and Competitiveness (grant FIS2012-36673-C03-01), and 'Grupos Consolidados UPV/EHU' program of the Basque Country Government (grant IT472-10). The work of E.Y.S. was also supported by the National Science Center in Poland as a research project No. DEC-2012/06/M/ST3/00042.

### Author contributions

J.R.B. prepared the samples, conducted the experiments with the help of M.P. and M.L., evaluated the data with the help of M.L., and wrote the first version of the manuscript together with M.M.; E.Y.S. supported the evaluation of the data and provided the analytic theory to determine Rashba disorder, spin dephasing and spin diffusion length; J.U.

provided the exact diagonalization results; M.M. and E.Y.S. devised the overall idea of the experiment. All authors contributed to the interpretation of the data and revising the manuscript.

### Additional information

Supplementary information is available in the [online version of the paper](#). Reprints and permissions information is available online at [www.nature.com/reprints](http://www.nature.com/reprints). Correspondence and requests for materials should be addressed to M.M.

### Competing financial interests

The authors declare no competing financial interests.

## Methods

**Preparation of clean InSb(110) surface.** InSb single crystals were glued with a conductive epoxy onto a molybdenum sample holder. A 1 mm deep notch was cut into the crystal to support cleaving along the (110) surface. A small screw was glued on top of the crystal. Inside an ultrahigh vacuum (UHV) chamber, at a base pressure of  $10^{-10}$  mbar, the crystal was cleaved at the notch by pushing the screw towards the chamber wall. After *in-situ* transfer into an in-house-built STM within one hour and direct cooling to 9 K, 4 K, 1.5 K, and 400 mK, respectively, atomically clean and flat terraces with widths of several  $\mu\text{m}$  were found.

**2DES inversion layer.** The cleaved surface of the p-doped InSb with acceptor density  $N_A = 1 \times 10^{24} \text{ m}^{-3}$  was transferred in UHV into a sample stage held at  $T = 30 \text{ K}$ , and Cs was evaporated from a Cs dispenser onto the surface. The Cs dispenser, operated at  $470^\circ \text{C}$ , contains caesium chromate. After three evaporation cycles of 180 s, the surface coverage is 1.8% of a monolayer of Cs, as determined by counting the Cs atoms. One monolayer is defined as one Cs atom per InSb unit cell (that is, there is one Cs atom for approximately 60 InSb unit cells or the Cs atoms are on average about 4 nm apart). These Cs atoms are surface donors inducing the 2DES<sup>28</sup>. The density of Cs is chosen to be relatively high, such that the positively charged Cs barely contributes to the potential fluctuations  $V_{2D}(\mathbf{R})$  (ref. 32). Estimates in Supplementary Section 7 reveal that Cs contributes  $\sim 1.5 \text{ meV}$  to the potential fluctuations of the 2DES, whereas the bulk acceptors contribute  $\sim 25 \text{ meV}$ . During the whole preparation, the pressure did not exceed  $1.6 \times 10^{-9}$  mbar. After the evaporation process, the sample was immediately transferred into the STM and cooled down.

**Peak fitting for determination of  $\epsilon_{0,-}$ ,  $\epsilon_{1,+}$ ,  $V_{2D}(\mathbf{R})$ , and spin splitting.** To discriminate the two spin levels of the lowest Landau level, we fit a double Lorentzian peak to the LDOS curves according to

$$\text{LDOS}(E) = \frac{a_1}{\pi} \frac{\sigma_1}{\sigma_1^2 + (E - \epsilon_{0,-})^2} + \frac{a_2}{\pi} \frac{\sigma_2}{\sigma_2^2 + (E - \epsilon_{1,+})^2} \quad (3)$$

with amplitudes  $a_{1,2}$ , peak widths  $\sigma_{1,2}$ , and peak energies  $\epsilon_{0,-}$  and  $\epsilon_{1,+}$  for peak 1 and 2, respectively. Whereas for  $B > 3.5 \text{ T}$  all six parameters are chosen to be free, for lower  $B$ ,  $\sigma_{1,2}$  were both fixed to 5.6 meV to deal with the less pronounced spin splitting. This is justified, because the distance of the two levels to  $E_F$  barely changes, leading to similar lifetimes and, thus, similar peak widths.

To first order, the LLs probe the electrostatic potential with a resolution approximately equal to the cyclotron radius (Supplementary Information 9). The electrostatic potential  $V_{2D}(\mathbf{R})$  is, thus, given by the average of  $\epsilon_{0,-}$  and  $\epsilon_{1,+}$  determined at the position  $\mathbf{R}$  with a precession of 1 meV (Supplementary Information 9). The spin splitting is the difference between  $\epsilon_{0,-}$  and  $\epsilon_{1,+}$ . Changes in the respective potential and in the spin splitting are not expected on a length scale shorter than  $l_B = 10.5 \text{ nm}$  at  $B = 6 \text{ T}$ , hence we smoothed both maps with a Gaussian curve of width  $l_B$ .

**Expected fluctuations of the Rashba coupling.** Here, we present analytical estimates of the random Rashba coupling and corresponding correlation lengths based on the approach developed in ref. 35, to compare with the experimental results. The model has no fitting parameters—that is, all inputs are known either from the experiment or from independent calculations and modelling. We use the experimentally determined densities of surface Cs atoms and bulk acceptors, as well as the electron density distribution along the  $z$ -axis as input parameters. Within our model, fluctuations in the spin–orbit coupling appear as a result of random electric fields of the negatively charged acceptors in the inversion layer and the positively charged Cs ions at the surface. For the random charge density we consider a random 2D distribution for positive charges and a random 3D distribution for negative charges.

We take the electron probability density distribution (see Fig. 1b)  $|\Psi_1(z)|^2$  as<sup>36</sup>:

$$|\Psi_1(z)|^2 = \frac{b^3}{2} z^2 \exp(-bz)$$

with the maximum position at  $z_0 = 5 \text{ nm}$ , corresponding to  $b = 0.4 \text{ nm}^{-1}$ . The local value of the spin–orbit coupling is produced by averaging the  $z$ -component of the electric field over the given probability density  $|\Psi_1(z)|^2$ .

As a result of having two sources of the electric field fluctuations, we obtain two 2D correlation functions of the Rashba parameters:

$$\langle \delta\alpha_{R,2D}(\mathbf{0}) \delta\alpha_{R,2D}(\mathbf{R}) \rangle = \langle (\delta\alpha_{R,2D})^2 \rangle F_{2D}(\mathbf{R}) \quad (4)$$

$$\langle \delta\alpha_{R,3D}(\mathbf{0}) \delta\alpha_{R,3D}(\mathbf{R}) \rangle = \langle (\delta\alpha_{R,3D})^2 \rangle F_{3D}(\mathbf{R}) \quad (5)$$

Here,  $F_{2D}(\mathbf{R})$  and  $F_{3D}(\mathbf{R})$  are the corresponding range functions. They can be calculated straightforwardly using lengthy integral expressions for corresponding correlators. The subscript 2D is used for the contribution of the surface Cs donors with the mean density  $\bar{n}_{2D}$  and the subscript 3D is used for that of the bulk

acceptors with the mean density  $\bar{n}_{3D}$ . We assume an uncorrelated white-noise distribution of dopants, both on the surface and in the bulk, described by:

$$\langle n_{2D}(\mathbf{0}) n_{2D}(\mathbf{R}) \rangle = \bar{n}_{2D} \delta(\mathbf{R}), \quad \langle n_{3D}(\mathbf{0}) n_{3D}(\mathbf{r}) \rangle = \bar{n}_{3D} \delta(\mathbf{r}) \quad (6)$$

where  $\mathbf{r}$  is a 3D coordinate. These densities of charged particles produce, at a point  $\mathbf{r}$ , a random electric field with an unscreened  $z$ -component in the form<sup>36</sup>

$$E_z(\mathbf{r}) = \frac{1}{4\pi\epsilon_0\epsilon_r\text{InSb}} e \left[ 2 \int n_{2D}(\mathbf{R}) \frac{\mathbf{r}-\mathbf{R}}{|\mathbf{r}-\mathbf{R}|^3} d^2R - \int n_{3D}(\mathbf{r}') \frac{\mathbf{r}-\mathbf{r}'}{|\mathbf{r}-\mathbf{r}'|^3} d^3r' \right]_z$$

where  $d^3r'$  integration is taken over the depletion layer ( $\epsilon_0$ : vacuum dielectric constant). We assume that the dielectric constant is  $\epsilon_r = 0.5\epsilon_{r,\text{InSb}}$  for positive Cs, because the Cs is surrounded by vacuum in the upper half-space, and  $\epsilon_r = \epsilon_{r,\text{InSb}}$  for negative acceptor charges, located in the bulk. Details of the coordinate dependence of the dielectric constant do not have a considerable effect on our results.

By averaging the products  $\langle E_z(\mathbf{r}_i) E_z(\mathbf{r}_j) \rangle$  over the disorder using the distribution  $|\Psi_1(z)|^2$  and the above presented white-noise correlators of the concentrations, one obtains<sup>35</sup>, after a lengthy but straightforward calculation, the correlation functions of the random contribution to the Rashba parameters. The variations of the spin–orbit coupling have the form

$$\langle (\delta\alpha_{R,2D})^2 \rangle^{1/2} = \left( \frac{2}{4\pi\epsilon_0\epsilon_r\text{InSb}} e^2 \xi \right) \times b \left( \frac{\pi}{10} \bar{n}_{2D} \right)^{1/2} \quad (7)$$

$$\langle (\delta\alpha_{R,3D})^2 \rangle^{1/2} = \left( \frac{1}{4\pi\epsilon_0\epsilon_r\text{InSb}} e^2 \xi \right) \times \left( \frac{\pi}{2} \bar{n}_{3D} b \right)^{1/2} \quad (8)$$

where the material-dependent constant  $\xi$  describes the proportionality between the electric field and the Rashba parameter<sup>37</sup>. The corresponding correlation lengths  $L_{2D(3D)}$  are defined as

$$L_{2D(3D)}^2 = 2\pi \int_0^\infty F_{2D(3D)}(R) R dR$$

using the dimensionless range functions  $F_{2D}(R)$  and  $F_{3D}(R)$  from equations (4) and (5).

This results in

$$L_{2D}^2 = \frac{40\pi}{b^2}, \quad L_{3D}^2 = \frac{\pi}{2} \cdot \frac{D_l}{b}$$

where  $D_l$  is the depletion layer depth. Note that because the  $\delta$ -functions of equation (6) do not have a characteristic nonzero spatial scale, the correlation length of the electric fields produced by the surface charges,  $L_{2D}$ , depends solely on the width of  $|\Psi_1(z)|^2$  (that is,  $1/b$ ). However, the bulk dopants are characterized, in addition, by the  $D_l$  spatial scale. As a result,  $L_{3D}$  includes two length parameters and increases only as the square root with  $D_l$  as the far-distant ions produce relatively weak fluctuations of the electric fields. The independence of  $\langle (\delta\alpha_{R,3D})^2 \rangle^{1/2}$  from the depletion layer depth in the  $D_l b \gg 1$  limit is shown by equation (8). It is interesting to mention that both correlation lengths depend solely on the system geometry and not on the material and sample parameters, such as  $\epsilon_r$ ,  $\xi$ , and the charge densities.

Substituting the characteristic numbers for the InSb inversion layer used in the experiment:  $\xi = 526 \text{ \AA}^2$  (ref. 37),  $\bar{n}_{2D} = 6 \times 10^{16} \text{ m}^{-2}$ ,  $\bar{n}_{3D} = 10^{24} \text{ m}^{-3}$ ,  $\epsilon_{r,\text{InSb}} = 16.8$  for the dielectric constant of InSb, and  $D_l = 30 \text{ nm}$  for the depletion layer width, we obtain  $\delta\alpha_R := \langle (\delta\alpha_{R,2D})^2 \rangle^{1/2} \approx \langle (\delta\alpha_{R,3D})^2 \rangle^{1/2} \approx 0.25 \text{ eV \AA}$  for the variations and  $L_{2D} \approx 28 \text{ nm}$ ,  $L_{3D} \approx 11 \text{ nm}$  for the correlation lengths, respectively. These numbers, being approximate, show a reasonable agreement with the experiment ( $\delta\alpha_R = 0.15 \text{ eV \AA}$ ,  $L_{R\alpha_{R}} = 30 \text{ nm}$ ) and allow us to attribute the experimental results to the fluctuations in the electric fields produced by randomness in the distribution of dopants. Notice that the variation in the calculated Rashba parameter due to the acceptors would be smeared in the experiment because the calculated  $L_{3D}$  is close to the value of the magnetic length  $l_B$ .

**Spin dephasing by random Rashba coupling.** Here we present the characteristic values of the length scales related to spin propagation in our experiment. The conventional D'yakonov–Perel' (DP) mechanism describes spin relaxation in a uniform Rashba field due to random spin precession directions between the scattering events. The Elliott–Yafet (EY) mechanism describes spin relaxation due to the spin flip at the scattering events. In contrast, the spin relaxation by the random Rashba field does not require any scattering. Thus, the corresponding spin relaxation rate is simply proportional to the correlation length of the Rashba disorder.

Taking the electron concentration  $n \approx 1 \times 10^{16} \text{ m}^{-2}$ , we obtain the Fermi wavevector  $k_F = \sqrt{2\pi n} \approx 3 \times 10^8 \text{ m}^{-1}$  and the corresponding Fermi velocity  $v_F = \hbar k_F / m^* \approx 1 \times 10^6 \text{ m s}^{-1}$ , using  $m^* = 0.03 m_e$ . Spin dephasing is given by the deviation from the regular precession due to the average Rashba effect within the random Rashba field. It has been calculated for the case in which DP and EY mechanisms are absent and only the disorder in the  $\alpha_R(\mathbf{R})$  parameter causes

dephasing<sup>35</sup>. The spin dephasing length—that is, the length that an electron travels on a random path before losing its spin memory—reads as ( $m^* = 0.03m_e$ ,  $\delta\alpha_R = 0.15$  eV Å,  $L_{\alpha_R\alpha_R} = 30$  nm):

$$l_{\text{Spin}} = \left( \frac{\hbar^2}{2m^*\delta\alpha_R} \right)^2 \frac{1}{L_{\alpha_R\alpha_R}} \approx 250 \text{ nm} \quad (9)$$

It is larger than the spin precession length  $l_{\text{SO}} = \pi\hbar^2/m^*\bar{\alpha}_R = 80$  nm. Most likely, it is also larger than the mean free path in our 2DES  $l_{\text{MFP}}$ . The mobility of the adsorbate-induced 2DES within an InSb(110) inversion layer has been measured at an acceptor density of  $\bar{n}_{\text{SD}} = 10^{21} \text{ m}^{-3}$  to be  $\mu = 1\text{--}10 \text{ m}^2 \text{ V}^{-1} \text{ s}^{-1}$  (ref. 34) leading to  $l_{\text{MFP}} = \hbar k_F \mu / e = 0.2\text{--}2 \mu\text{m}$ . As the acceptor distance within our sample is a factor of ten lower, we estimate  $l_{\text{MFP}} \approx 20\text{--}200$  nm. Thus, the spin propagation in our

sample is diffusive, with an estimated spin diffusion length  $l_s$ , which is the effective propagation distance of electrons within a sample before dephasing:

$$l_s = \sqrt{l_{\text{Spin}} l_{\text{MFP}} / 2} \approx 50\text{--}150 \text{ nm} \quad (10)$$

**Data availability.** The data that supports the plots within this paper and other findings of this study are available from the corresponding author on request.

## References

36. Ando, T., Fowler, A. B. & Stern, F. Electronic properties of two-dimensional systems. *Rev. Mod. Phys.* **54**, 437–672 (1982).
37. Winkler, R. *Springer Tracts in Modern Physics* (Springer, 2003).